Dark matter–radiation interactions: the impact on dark matter haloes

J. A. Schewtschenko,[1,2]★ R. J. Wilkinson,[2] C. M. Baugh,[1] C. Bœhm[2,3] and S. Pascoli[2†]

[1]*Institute for Computational Cosmology, Durham University, Durham DH1 3LE, UK*
[2]*Institute for Particle Physics Phenomenology, Durham University, Durham DH1 3LE, UK*
[3]*LAPTH, U. de Savoie, CNRS, BP 110, F-74941 Annecy-Le-Vieux, France*

ABSTRACT

Interactions between dark matter (DM) and radiation (photons or neutrinos) in the early Universe suppress density fluctuations on small mass scales. Here, we perform a thorough analysis of structure formation in the fully non-linear regime using *N*-body simulations for models with DM–radiation interactions and compare the results to a traditional calculation in which DM only interacts gravitationally. Significant differences arise due to the presence of interactions, in terms of the number of low-mass DM haloes and their properties, such as their spin and density profile. These differences are clearly seen even for haloes more massive than the scale on which density fluctuations are suppressed. We also show that semi-analytical descriptions of the matter distribution in the non-linear regime fail to reproduce our numerical results, emphasizing the challenge of predicting structure formation in models with physics beyond collisionless DM.

Key words: astroparticle physics – galaxies: haloes – dark matter – large-scale structure of Universe.

1 INTRODUCTION

Dark matter (DM) is the most dominant and yet most elusive component of matter in the Universe. Exploring its nature is therefore one of the greatest challenges in both cosmology and particle physics today. The usual treatment of DM in structure formation (SF) calculations neglects possible interactions between DM and other species. Yet if DM is a (thermal) weakly interacting massive particle (WIMP), interactions (and more precisely, annihilations) are essential to obtain the correct relic density. It is therefore important to study the impact of DM interactions on other cosmological observables.

It has been already established that a DM coupling with primordial radiation, i.e. photons (Boehm, Fayet & Schaeffer 2001; Boehm et al. 2002; Sigurdson et al. 2004; Boehm & Schaeffer 2005; Dolgov et al. 2013; Wilkinson, Boehm & Lesgourgues 2014a) or neutrinos (Boehm et al. 2001, 2002; Boehm & Schaeffer 2005; Mangano et al. 2006; Serra et al. 2010; Wilkinson, Boehm & Lesgourgues 2014b) leaves a characteristic imprint on the cosmic microwave background (CMB) temperature and polarization power spectra. In addition, in a previous publication (Boehm et al. 2014), we showed using *N*-body simulations that such interactions have a significant impact on the Milky Way environment, dramatically reducing the number of DM subhaloes that could potentially host satellite galaxies.[1] Since they have the potential to alleviate the small-scale problems that have persisted in the standard cold DM (CDM) model for more than a decade (Klypin et al. 1999; Moore et al. 1999; Boylan-Kolchin, Bullock & Kaplinghat 2011), these interactions should not be ignored.

We now go a step further and study the abundance and properties, such as shape, spin and density profile of collapsed DM structures in the presence of DM–radiation interactions. We highlight the differences with respect to CDM and in addition, warm DM (WDM), which shows a qualitatively similar suppression of power on small scales (Schaeffer & Silk 1988). We note that recent work has also considered non-linear SF in a number of alternative models such as self-interacting DM (Rocha et al. 2013; Vogelsberger et al. 2014), decaying DM (Wang et al. 2014), late-forming DM (Agarwal et al. 2014), atomic DM (Cyr-Racine & Sigurdson 2013) and DM interacting with dark radiation (Buckley et al. 2014; Chu & Dasgupta 2014); see also Schneider (2014).

The paper is organized as follows. In Section 2, we summarize the theoretical background and results obtained thus far using linear perturbation theory. In Section 3, we describe the setup of our numerical simulations. In Sections 4 and 5, we analyse the abundance and properties of the collapsed structures, comparing our results with semi-analytical approximations from the literature. Our conclusions are presented in Section 6.

★E-mail: j.a.schewtschenko@dur.ac.uk
†Also visiting Instituto de Física Teórica, IFT-UAM/CSIC, Universidad Autónoma de Madrid, Cantoblanco, 28049, Madrid, Spain.

[1] See also Bertoni et al. (2014).
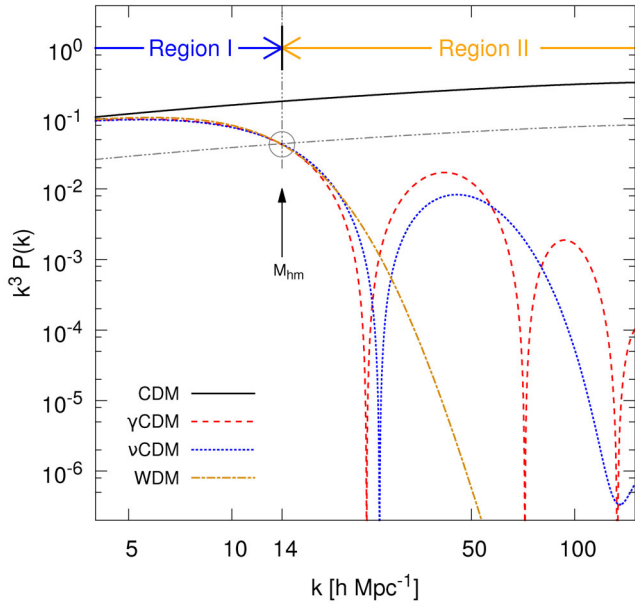
Figure 1. The linear matter power spectra for collisionless CDM (solid, black), γCDM (dashed, red), νCDM (dotted, blue) and WDM (dash–dotted, orange) at redshift $z = 49$. The interaction cross-sections for γCDM and νCDM and the particle mass for WDM have been selected such that the initial suppression with respect to CDM is identical (see Table 1). This wavenumber defines the half-mode mass, $M_{\rm hm}$, which is marked with an arrow and separates regions I and II, which are discussed with reference to Fig. 2.

2 THEORETICAL BACKGROUND

Among all the possible contributions to the collisional damping of DM fluctuations, the largest occurs when DM interacts with photons (γCDM) or neutrinos (νCDM). There are two reasons for this: (i) photons and neutrinos have the largest energy density of any standard model particle until matter–radiation equality, (ii) they are relativistic and therefore tend to drag DM particles out of small mass overdensities if they are coupled to DM.

For large values of the DM–radiation scattering cross-section, the suppression is prominent in both the CMB temperature and polarization power spectra. A comparison between the predicted spectra and the first-year data from *Planck* (Planck Collaboration XVI 2014) gives upper bounds of $8 \times 10^{-31}(m_{\rm DM}/{\rm GeV}){\rm cm}^2$ and $2 \times 10^{-28}(m_{\rm DM}/{\rm GeV}){\rm cm}^2$ on the γCDM and νCDM cross-sections, respectively, where $m_{\rm DM}$ is the DM particle mass (at 68 per cent CL, assuming a constant cross-section; Wilkinson et al. 2014a,b).

The reason why these constraints differ for γCDM and νCDM is that photons and neutrinos do not have exactly the same effect on DM fluctuations due to their different thermal histories, with photons staying coupled to the thermal bath for much longer due to Thomson scattering.[2] Their effect on the matter power spectrum is also different, as illustrated in Fig. 1, where we show the linear theory matter power spectra for collisionless CDM, γCDM, νCDM and (collisionless) WDM.

Unless explicitly stated otherwise, the values we use throughout this paper for the γCDM and νCDM cross-sections and the WDM

Table 1. The (constant) elastic scattering cross-sections for γCDM and νCDM and the particle mass for WDM, expressed in various units. $\sigma_{\rm Th}$ is the Thomson cross-section, $m_{\rm DM}$ is the DM mass and α is defined in equation (2). Note that the mass of the WDM particle is motivated by the reproduction of the half-mode mass in the γCDM and νCDM models, as explained in the text.

	$(m_{\rm DM}/{\rm GeV})$ $\times \sigma_{\rm Th}$	$(m_{\rm DM}/{\rm GeV})$ $\times {\rm cm}^2$	$(m_{\rm DM}/{\rm g})$ $\times {\rm cm}^2$
γCDM	2.0×10^{-9}	1.3×10^{-33}	7.5×10^{-10}
νCDM	2.9×10^{-9}	1.9×10^{-33}	1.1×10^{-9}
	$m_{\rm DM}$ (keV)	α (h^{-1} Mpc)	
WDM	1.2	0.037	

mass are given in Table 1. These parameters are motivated by the constraints obtained in our previous work (Boehm et al. 2014) and have been selected such that the scale at which the transfer function is suppressed by a factor of 2 with respect to CDM (hence giving a factor of 4 reduction in power) is identical. This scale defines the *half-mode* mass, $M_{\rm hm}$, and demarks the range of wavenumbers labelled as regions I and II in Fig. 1. In region II, there are important differences between the power spectra for γCDM, νCDM and WDM.

In the case of a thermalized, non-interacting, fermionic WDM particle, the suppression in the matter power spectrum is typically approximated by the transfer function (Bode, Ostriker & Turok 2001)

$$T(k) = \left[1 + (\alpha k)^{2\mu} \right]^{-5/\mu} , \tag{1}$$

where

$$\alpha = 0.048 \left[\frac{m_{\rm DM}}{\rm keV} \right]^{-1.15} \left[\frac{\Omega_{\rm DM}}{0.4} \right]^{0.15} \left[\frac{h}{0.65} \right]^{1.3} \frac{\rm Mpc}{h} . \tag{2}$$

Here, $\Omega_{\rm DM}$ is the DM energy density, h is the reduced Hubble parameter and $\mu \simeq 1.2$ is a fitting parameter.[3] The scale α in equation (2) encapsulates the effect of free-streaming, which erases primordial fluctuations below a wavelength given by

$$\lambda_{\rm fs} = \int_{t_{\rm dec}}^{t_0} \frac{v(t)}{a(t)} {\rm d}t \approx r_{\rm H}(t_{\rm NR}) \left[1 + \frac{1}{2} \log \left(\frac{t_{\rm EQ}}{t_{\rm NR}} \right) \right] , \tag{3}$$

where $v(t)$ is the thermal velocity of the WDM particle. In this expression, $t_{\rm dec}$ is the DM decoupling time, t_0 is the time today, $a(t)$ is the cosmological scalefactor, $r_{\rm H}(t_{\rm NR})$ is the comoving size of the horizon when DM becomes non-relativistic (at time $t_{\rm NR}$) and $t_{\rm EQ}$ is the epoch of matter–radiation equality.

A similar transfer function can be used to model the cut-off in the matter power spectra in γCDM and νCDM (Boehm et al. 2002) with

$$\tilde{\alpha} = \beta_X \left[\frac{\sigma_{{\rm DM}-X}}{\sigma_{\rm Th}} \frac{m_{\rm DM}}{\rm GeV} \right]^{0.48} \left[\frac{\Omega_{\rm DM}}{0.4} \right]^{0.15} \left[\frac{h}{0.65} \right]^{1.3} \frac{\rm Mpc}{h} , \tag{4}$$

where X is γ or ν, $\beta_\gamma \approx 1.25 \times 10^4$, $\beta_\nu \approx 1.04 \times 10^4$, $\sigma_{{\rm DM}-X}$ is the DM–radiation cross-section and $\sigma_{\rm Th}$ is the Thomson cross-section. This transfer function fixes the half-mode scale for γCDM and νCDM, thus providing a means to compare the impact of the interactions with respect to WDM, but does not encapsulate the full suppression of the power spectrum.

---

[2] In addition, γCDM has a direct impact on the CMB, while νCDM only affects the CMB indirectly, and the parameter space for νCDM suffers from significant degeneracies (see Wilkinson et al. 2014b).

[3] There is an alternative fit for α and μ that is often used in the literature (e.g. Viel et al. 2005), but the difference is marginal for our analysis.

Equation (4) corresponds to an analytical calculation of the collisional damping scale given by[4]

$$\lambda_{cd}^2 = \frac{2\pi^2}{3} \int_0^{t_{dec}} \frac{\rho_X}{\not\rho} \frac{v_X^2 (1 + \Theta_X)}{a^2 \Gamma_X} \, dt. \tag{5}$$

In this equation, $\not\rho = \rho_X + p_X$, where ρ_X is the energy density, p_X the pressure, v_X is the velocity dispersion and Γ_X is the total interaction rate of the DM interaction partner and Θ_X contains the contribution from heat conduction.

As the integral in equation (5) is dominated by the contribution at late times, the collisional damping scale can be approximated by

$$\lambda_{cd}^2 \approx \frac{2\pi^2}{3} \left[\frac{\rho_X}{\not\rho} \frac{v_X^2 (1 + \Theta_X)}{a^2} \frac{t^2}{\alpha_X} \right]\Bigg|_{t_{dec}}, \tag{6}$$

using $\Gamma_X = H = \alpha_X/t$ at $t = t_{dec}$, where H is the Hubble rate, $\alpha_X = 1/2$ if $t_{dec} < t_{EQ}$ and $\alpha_X = 2/3$ otherwise. On scales smaller than λ_{cd}, primordial fluctuations are erased.

We summarize the impact of the damping scales λ_{fs} and λ_{cd} in linear theory in Fig. 2. To distinguish these quantities from the half-mode mass scale, M_{hm}, we present the mass corresponding to the relevant damping scale as a function of the DM mass (for WDM) and interaction cross-section (for γCDM and νCDM).

We identify three regions in Fig. 2. Regions I and II are already labelled in Fig. 1 and there is now an additional region (III) occurring at much higher wavenumbers than that are plotted in this figure. In region I, haloes form hierarchically, while in region III, all primordial perturbations have been erased. In between lies a transition region (region II), where some primordial density fluctuations may survive to form structure, but these are already sufficiently suppressed to disfavour a typical hierarchical SF. Region II extends down to much smaller scales for γCDM and νCDM compared to WDM due to the prominent oscillations in the matter power spectrum.[5] The separation between regions I and II is determined by the half-mode mass scale (as in Fig. 1), while the transition between regions II and III is governed by the free-streaming scale (for WDM) or collisional damping scale (for γCDM and νCDM).

3 SIMULATIONS

To calculate the non-linear evolution of the matter distribution, we run a suite of high-resolution *N*-body simulations using the parallel Tree-Particle Mesh code, GADGET-3 (Springel 2005). To model a wide dynamical range, we perform simulations in large boxes (of side lengths 100 and 300 h^{-1} Mpc) and a small box (of side length 30 h^{-1} Mpc), all containing 1024^3 particles.

The simulations begin at a redshift of $z = 49$ (the DM–radiation interaction rate is negligible for $z < 49$) and use a gravitational softening of 5 per cent of the mean particle separation. The initial conditions are created with an adapted version of a second-order LPT code (Crocce, Pueblas & Scoccimarro 2012), using input matter power spectra from a modified version of the Boltzmann code, CLASS (Lesgourgues 2011).

---

[4] We neglect the possible contributions from self-interactions and *mixed damping* and simplify the calculation to a single DM interaction partner.
[5] We note that acoustic oscillations are also expected in the transfer functions for certain WDM models at small scales (see e.g. Boyanovsky & Wu 2011). However, at these scales, the transfer function is already strongly suppressed by free-streaming so the regeneration of power from these oscillations is expected to be much weaker than in γCDM and νCDM.
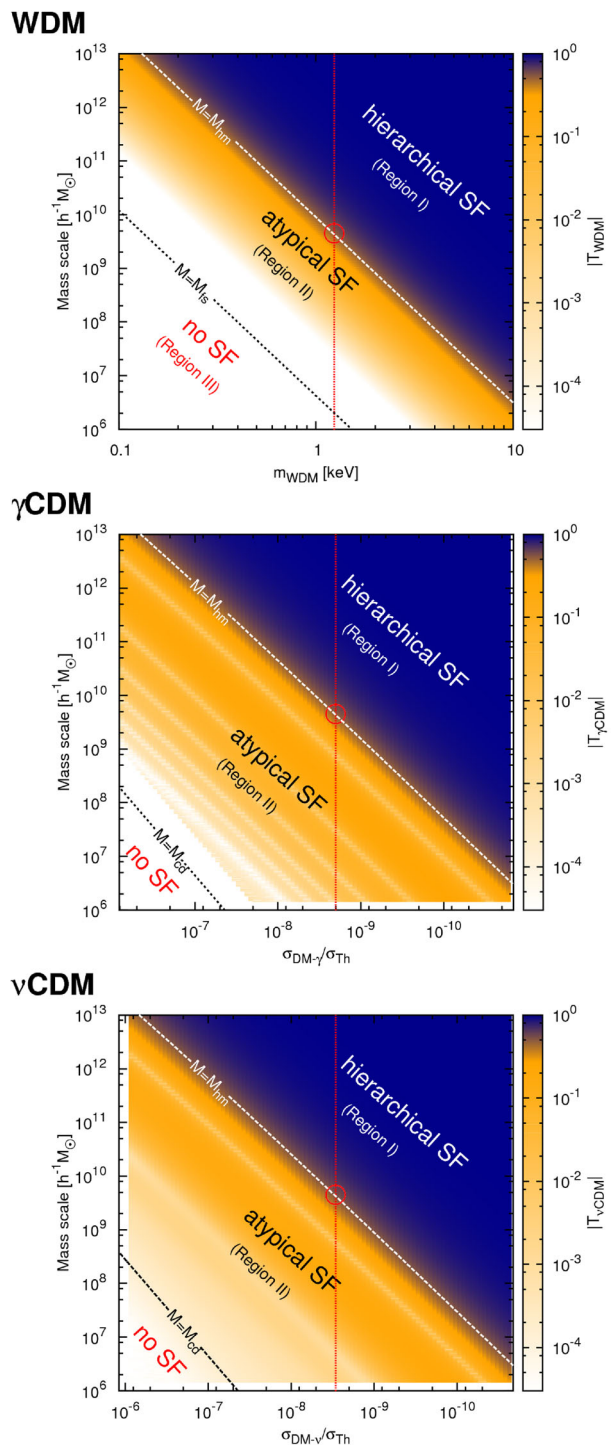
Figure 2. Characteristic mass scales for the suppression of primordial fluctuations by free-streaming (WDM, top), photon collisional damping (γCDM, middle) and neutrino collisional damping (νCDM, bottom). The half-mode mass scale, M_{hm}, is defined by the initial cut-off in the transfer function and marks the upper boundary of region II, where hierarchical SF may no longer occur due to a reduced number of low-mass progenitors. M_{fs} and M_{cd} are the masses corresponding to the free-streaming and collisional damping scales, respectively, and define the boundary of region III, where structures no longer form. The colour scale shows the absolute value of the transfer function, $T(k)$, and the vertical red lines correspond to the DM parameters listed in Table 1.

We use the best-fitting values of the cosmological parameters obtained by the *Planck* collaboration in the '*Planck* + WP' data set (Planck Collaboration XVI 2014), assuming a flat ΛCDM cosmology. In principle, a consistent treatment of an interacting DM model would require one to study each cross-section within its own best-fitting cosmology. However, we find that the parameters for ΛCDM lie within one standard deviation of such best fits. Therefore, we keep the cosmological parameters fixed for all the models studied here.

Lovell et al. (2014) showed that in the case of WDM, one can safely ignore thermal velocities, without introducing a significant error on the scales of interest, if the DM particle is heavier than ∼1 keV. We confirmed this by performing simulations with and without a thermal velocity dispersion and obtaining convergence on the scales of interest. Hence, we only consider models in which late-time free-streaming can be neglected.

Fig. 3 shows the projected DM distribution in the 30 h^{-1} Mpc box for (i) collisionless CDM and (ii) an extreme γCDM model that is allowed by *Planck* CMB data (Wilkinson et al. 2014a). Fewer small structures are present in γCDM as an immediate result of the suppression of small-scale power shown in Fig. 1. The only exception is found along the filaments, where spurious structures contaminate the otherwise smooth environment (Wang & White 2007). Similar results are obtained for νCDM and WDM.

For abundance measurements (Section 4), DM haloes are identified using a *friends-of-friends* group finder (Davis et al. 1985) with a linking length of 20 per cent of the mean particle separation. For the halo properties (Section 5), we instead use the AMIGA *halo finder* (Knollmann & Knebe 2009), where collapsed structures are defined as spherically overdense regions of radius r_{vir} with a mean density given by

$$\frac{3M_{\text{vir}}}{4\pi r_{\text{vir}}^3} = \Delta_{\text{th}}\rho_{\text{crit}}. \tag{7}$$

In this expression, M_{vir} is the virial mass, ρ_{crit} is the critical density and Δ_{th} is the mean overdensity of a virialized halo with respect to the critical density, according to the spherical top-hat collapse model.

4 RESULTS: HALO ABUNDANCE

The suppression of small-scale density fluctuations in the early Universe (as discussed in Section 2) has a significant effect on the subsequent SF. This has been studied in detail for WDM (e.g. Lovell et al. 2014), where the halo mass function (HMF) was compared to semi-analytical predictions. In this section, we perform a similar analysis for γCDM and νCDM by comparing the simulated HMFs with the *Press–Schechter* formalism (Press & Schechter 1974) and modifications thereof. In addition, we study the spatial distribution of DM haloes on large scales.

4.1 Semi-analytical HMFs

The *Press–Schechter* formalism uses the known primordial perturbations and their linear growth to calculate the fractional volume of space occupied by virialized objects of a given mass, assuming a spherical collapse model (Press & Schechter 1974). The HMF can be written as

$$\frac{\text{d}n(M)}{\text{d}M} = -\frac{1}{2} f^{(\text{HMF})}(\sigma^2) \frac{\bar{\rho}}{M^2} \frac{\text{d}\ln\sigma^2(M)}{\text{d}\ln M}, \tag{8}$$

where $n(M)$ is the number density of DM haloes of mass $M \to M + \text{d}M$, $\bar{\rho}$ is the average matter density of the Universe and $\sigma^2(M)$ is the variance of the linear density field given by

$$\sigma^2(M) = \frac{1}{2\pi^2} \int_0^\infty k^2 P(k)\hat{W}^2(k, R)\,\text{d}k. \tag{9}$$

The variance is smoothed on a mass-dependent scale $R(M)$, using a suitable window function $W(r, R)$, which has a Fourier transform $\hat{W}(k, R)$ (Jenkins et al. 2001).

The *Sheth–Tormen* (ST) formalism (Sheth, Mo & Tormen 2001) combines the Press–Schechter formalism with an ellipsoidal collapse model. In this model, the function $f^{(\text{HMF})}(\sigma^2)$ in equation (8) represents the fraction of collapsed haloes and is defined by

$$f_{\text{ST}}^{(\text{HMF})}(\sigma^2) = A\sqrt{\frac{2}{\pi}}\left[1 + x^{-2p}\right]x\exp\left[-x^2/2\right]. \tag{10}$$

In this expression, $x \equiv \sqrt{a}\delta_c/\sigma$, where δ_c is the cosmology-dependent linear overdensity at the time of collapse. The parameters $A \approx 0.3222$, $p \approx 0.3$ and $a \approx 0.707$ were obtained by fitting to simulation results (Sheth et al. 2001).

The window function, $W(r, R)$, is in general, arbitrary. However, certain choices of window function are advantageous as they allow for both a sensible definition of the smoothed density field and an semi-analytical solution for the Fourier transform. A real-space top-hat, $W(r, R) = \Theta(1 - |r/R|)$, has the advantage of a well-defined smoothing scale, R, defined in terms of the halo mass, $M(R)$, as

$$R = \left(\frac{3M}{4\pi\bar{\rho}}\right)^{1/3}. \tag{11}$$

However, recent papers (Benson et al. 2013; Schneider, Smith & Reed 2013) have shown that this choice does not reproduce the HMF for cosmologies with a cut-off in the matter power spectrum at small scales. Instead, the predicted HMF continues to increase with decreasing M, while the suppression of primordial matter perturbations demands the opposite. The reason for this behaviour is illustrated in Fig. 4, where the Fourier-transformed real-space top-hat and (intermediate) steps of the HMF calculations are shown by red/dashed lines. For this type of window function, one obtains significant contributions from a wide range of unsuppressed larger scales, which dominate the resulting variance and thus, the predicted HMF.

A k-space top-hat window function is only sensitive to local changes in the matter distribution in k-space and thus reproduces the expected suppression in the halo abundance for damped power spectra (see Fig. 4, blue/solid lines). However, the mass-smoothing scale relation (M–R) must now be defined without the simple geometrical justification of equation (11), which was used in the real-space case.

Here, we use the definition of Lacey & Cole (1993), which defines the cut-off wavenumber, k_s, in relation to the mass, M, based on the normalization choice

$$k_s = \left(\frac{M}{6\pi^2\bar{\rho}}\right)^{-1/3}. \tag{12}$$

This corresponds to a correction factor of $c \equiv Rk_s \approx 2.42$ with respect to equation (11), so that the semi-analytical HMF matches numerical simulations at large scales.[6]

---

[6] Note that Schneider et al. (2013) and Benson et al. (2013) follow a very similar approach, but with slightly different values for c.
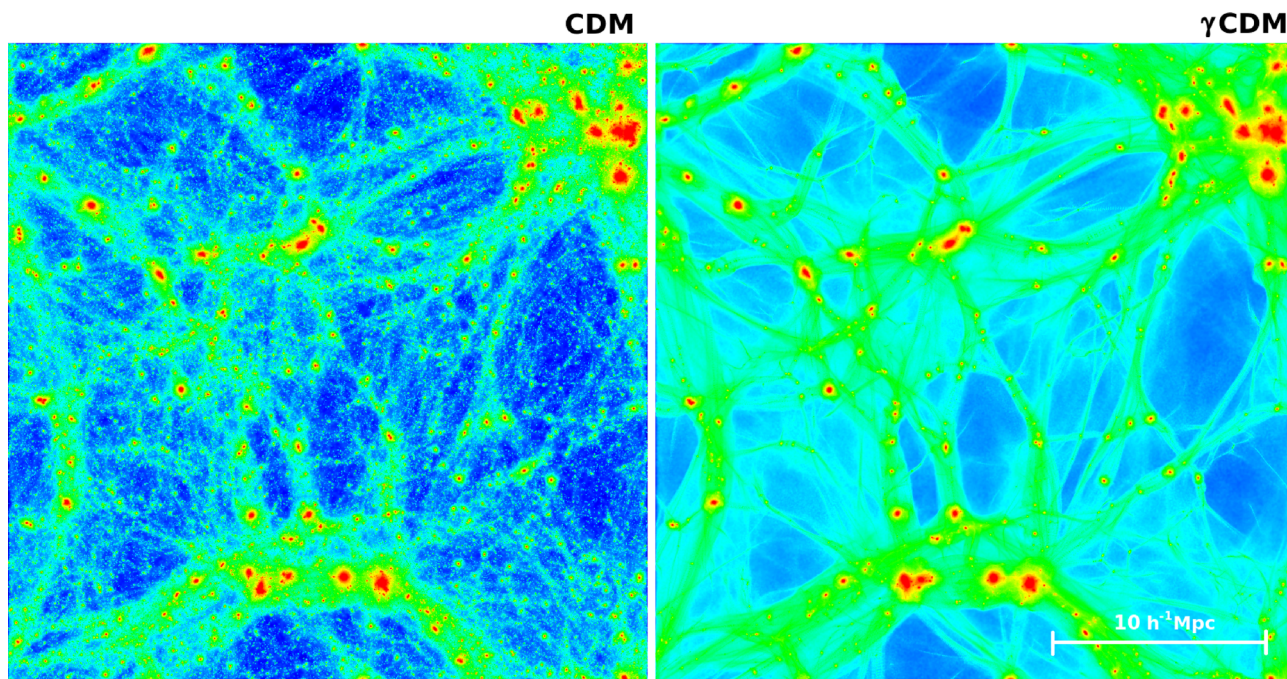
Figure 3. The simulated distribution of DM at redshift $z = 0$ in a box of side length 30 h^{-1} Mpc for two models: collisionless CDM (left) and γCDM with $\sigma_{DM-\gamma} = 10^{-7} \sigma_{Th} (m_{DM}/\text{GeV}$, right), which is allowed by *Planck* CMB data (Wilkinson et al. 2014a). The colours indicate the DM density on a scale increasing from blue to red. Due to collisional damping, we obtain fewer small-scale structures in γCDM than are seen in CDM.
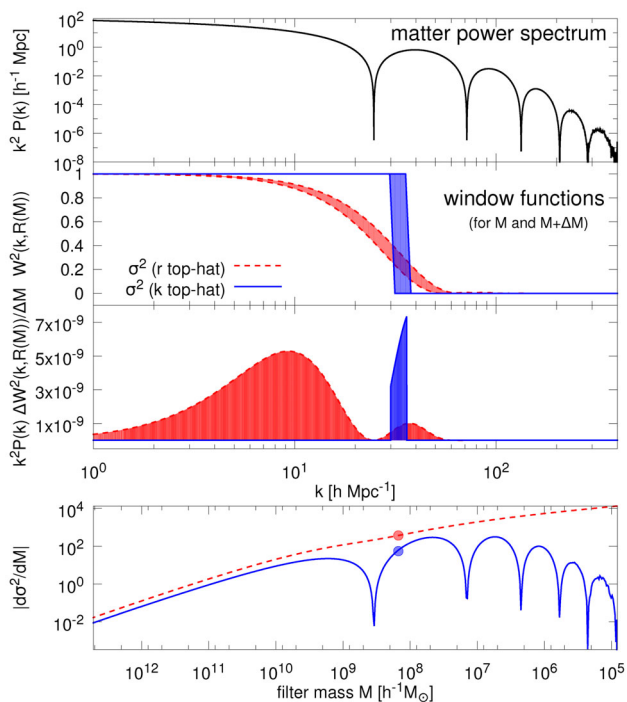
Figure 4. Real-space and k-space top-hat window functions in Press–Schechter HMF predictions for γCDM. The upper panel shows the matter power spectrum, while the second panel shows the Fourier transform of the two window functions (r top-hat and k top-hat). Each window function is evaluated for two filter masses, M and $M + \Delta M$. The difference between the two filter masses is highlighted by the shaded region in each case. The third panel shows the result of applying this differential filter to the matter distribution. Finally, the lower panel shows the integrated result for both window functions. The red and blue points are the results for the specific filter mass M used in the middle two panels.

Alternatively, Schneider et al. (2012) found that while the r-space top-hat did not match the results of their N-body simulations, an additional mass-dependent correction factor,

$$\frac{n(M)}{n^{ST}(M)} = \left(1 + \frac{M_{hm}}{\beta M}\right)^{-\alpha}, \tag{13}$$

could correct for this, where α and β are free parameters. Schneider et al. (2012) set $\beta = 1$ and found a best-fitting value of $\alpha = 0.6$. As discussed in the next section, we find better agreement with our simulation results by setting $\beta = 2$; we will refer to this version of equation (13) as the *modified* Schneider et al. correction.

4.2 Simulated HMF

We plot the differential HMFs measured in the collisionless CDM, γCDM, νCDM and WDM simulations in Fig. 5. We also show the predictions obtained using the semi-analytical approximations described in Section 4.1.

The mass function proposed by Schneider et al. (2012) predicts fewer haloes than are seen in collisionless CDM but nevertheless overestimates the abundance of haloes less massive than $\sim 10^{10.5} \, h^{-1} \, M_\odot$. Using a modified version of the Schneider et al. correction, with $\beta = 2$ instead of $\beta = 1$ extends the reproduction of the simulation results down to a halo mass of $\sim 10^{8.6} \, h^{-1} \, M_\odot$ for WDM. However, it does not reproduce the abundance of haloes seen in the simulations of γCDM and νCDM, underestimating the measured abundance of haloes at $10^{8.6} \, h^{-1} \, M_\odot$ by a factor of 2.

The clear upturn observed in the HMF at low masses in Fig. 5 (i.e. below $M_{vir} \lesssim 10^9 \, h^{-1} \, M_\odot$) is due to non-physical, spurious structures (Wang & White 2007). We try to avoid contamination from such artificial structures by only considering the mass function and halo properties for objects with masses far above this value.

A comparison between the simulated abundance of haloes in the four models and the semi-analytical predictions reveals significant
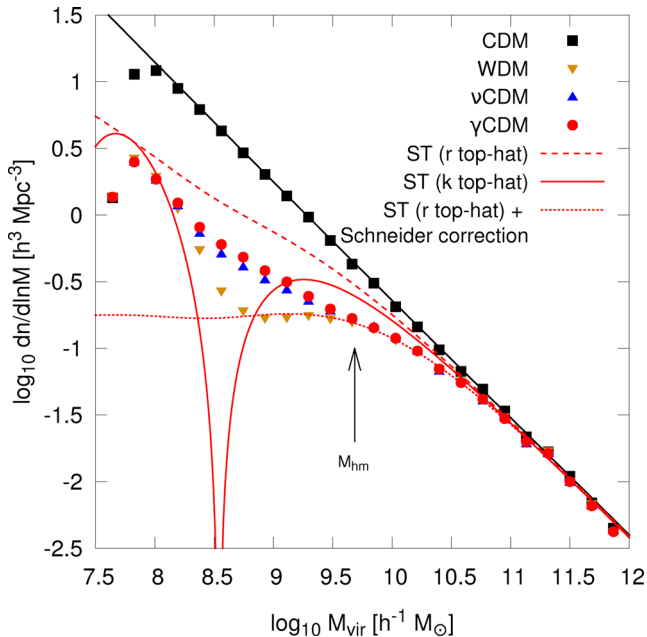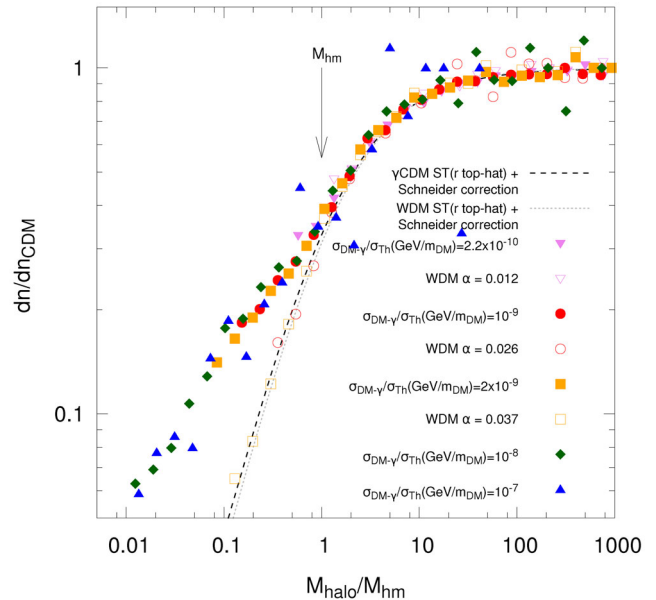
Figure 5. The HMFs for collisionless CDM, WDM, νCDM and γCDM at redshift $z = 0$. The HMF measured in models with damped power spectra contains contributions from spurious haloes, which dominate at the smallest masses and result in the upturn seen at $M_{\rm vir} \sim 10^9 \, h^{-1} \, {\rm M_\odot}$. Above this scale and below the half-mode mass, $M_{\rm hm}$ (marked by the arrow), the abundance of haloes in γCDM and νCDM exceeds that seen in WDM. Predictions using the ST formalism with a real-space (dashed) or k-space (solid) top-hat window function, as well as the modified Schneider et al. correction (dotted), are also shown. All the semi-analytical predictions fail to predict the HMFs for γCDM and νCDM.

Figure 6. The halo abundance expressed in units of the half-mode mass, $M_{\rm hm}$, for γCDM (filled symbols) and WDM (unfilled symbols), with respect to CDM, at redshift $z = 0$. The suppression in the HMF is universal with respect to the values of the γCDM cross-section and WDM particle mass. The result for WDM matches the semi-analytical prediction of a r-space top-hat with the Schneider et al. correction. However, we obtain more haloes in γCDM than in WDM as a result of the significant oscillations in the matter power spectrum. Hence, the modified ST HMF does not provide a good fit to our simulation results.

differences. The main feature, the reduced number of haloes in γCDM, νCDM and WDM, with respect to CDM, is a consequence of the damping of primordial fluctuations on small scales. There is also a larger number of low-mass structures in γCDM and νCDM, relative to WDM, due to the prominent oscillations in the power spectra of the former models, at wavenumbers larger than the scales on which fluctuations are suppressed.

A direct comparison between the γCDM and WDM models (see Fig. 6) reveals that in both cases, the suppression of the HMF follows a universal profile, if the halo mass is plotted normalized by the half-mode mass, $M_{\rm hm}$. An excess of haloes in γCDM with respect to WDM occurs at $M_{\rm hm}$ for all the cross-sections studied in this work. A similar result is found for νCDM.

The higher halo abundance seen in the γCDM and νCDM simulations compared to that found in WDM is difficult to explain since the primordial matter power spectra shown in Fig. 1 are very similar down to the wavenumber corresponding to the half-mode mass, $M_{\rm hm}$. There is a much stronger suppression in the γCDM and νCDM spectra than in WDM immediately below $M_{\rm hm}$. The scales where the power in γCDM and νCDM exceeds that in WDM correspond to halo masses that are an order of magnitude smaller than $M_{\rm hm}$, marked by the location of the first oscillation in the halo abundance for γCDM and νCDM, according to the ST formalism. Instead of showing a strong reduction in halo abundance below $M_{\rm hm}$, the simulated HMFs for γCDM and νCDM seem to bridge the gap between the primary power cut-off scale and the subsequent increase in the halo abundance resulting from the oscillating matter power spectra.

Given that the simulations for WDM, γCDM and νCDM use similar initial conditions (e.g. identical box size, phases, number

of particles), numerical errors can most likely be excluded as a possible explanation for this deviation. Therefore, this is a strong hint that the understanding of SF in the ST formalism, which works so well in the strictly hierarchical case, appears to fail when there is oscillating power in the initial matter distribution.

4.3 Halo bias

We determine the linear clustering bias of DM haloes, $b_{\rm lin}(M)$, using the ratio between the halo-density cross-correlation and the density–density autocorrelation on large scales (i.e. at small wavenumbers),

$$b_{\rm lin}(M) = \lim_{k \to 0} \frac{P_{\rm hm}(M)}{P_{\rm mm}} . \qquad (14)$$

Using the cross-correlation of haloes and mass rather than the autocorrelation of haloes reduces the impact of shot noise (see Angulo, Baugh & Lacey 2008).

To ensure that we recover the asymptotic value of $b_{\rm lin}(M)$, we use the largest simulation box of side length $300 \, h^{-1}$ Mpc. For large scales ($k \lesssim 0.1 \, h^{-1}$ Mpc), convergence is reached as the halo bias becomes constant. Therefore, we can replace the limit in equation (14) with the average over all scales larger than $k = 0.1 \, h^{-1}$ Mpc to reduce the impact of statistical fluctuations arising from the small number of high-mass haloes and low-wavenumber modes in the simulation box. This wavenumber scale corresponds to the largest mode in the $100 \, h^{-1}$ Mpc box and, as the shot noise fluctuations are less important for the more abundant low-mass DM haloes, we use the smaller box to measure the halo bias for masses below $10^{11} \, h^{-1} \, {\rm M_\odot}$.

We do not find a significant deviation from the bias expected in collisionless CDM for WDM, γCDM or νCDM, which agrees with the expectations from the semi-analytical models of halo bias. We

therefore conclude that the suppression of small-scale structure in the matter power spectra in γCDM and νCDM takes place independently of the linear background in both overdense and underdense regions. Thus, the clustering properties do not change on the mass scales probed here ($M \gtrsim 10^9 \, h^{-1} \, \mathrm{M_\odot}$).

5 RESULTS: HALO PROPERTIES

As seen in Section 4, DM–radiation interactions lead to a reduced abundance of low-mass DM haloes. In this section, we focus on three key properties of these haloes: their shape, density profile and spin.

For this analysis, it is important to only consider DM haloes that are dynamically relaxed. We apply the selection criteria presented in Maccio' et al. (2007) and Neto et al. (2007). The DM haloes must satisfy the following conditions.[7]

(i) *Centre-of-mass displacement*: the offset, s, between the halo centre of mass, r_{cm}, and the potential centre, r_{cp}, normalized by the virial radius, r_{vir}, satisfies

$$s = \|r_{cp} - r_{cp}\| < 0.07. \tag{15}$$

(ii) *Virial ratio*: the total kinetic energy of the halo particles within r_{vir} in the halo rest frame, T, and their gravitational potential energy, U, satisfies

$$2T/\|U\| < 1.35. \tag{16}$$

These criteria reduce the number of haloes in our sample by a factor of 2, but also significantly decrease the scatter as major mergers and their unrelaxed descendants are removed.

In addition to applying these conditions, our mass-averaged results are restricted to: (i) the subset of haloes with a virial mass smaller than $10^{11} \, h^{-1} \, \mathrm{M_\odot}$, i.e. the mass range that shows a suppression in the halo abundance, and (ii) in order to avoid resolution problems, larger than 1000 particles, i.e. mass bins larger than $\sim 10^{9.3} \, h^{-1} \, \mathrm{M_\odot}$. The latter criterion ensures that the estimates for our observables have converged (Power et al. 2003). This lower limit also minimizes the possibility of contamination by spurious structures as they form and mainly affect haloes on small mass scales ($M \lesssim 10^9 \, h^{-1} \, \mathrm{M_\odot}$); this can be checked by studying their contribution to the HMF plotted in Fig. 5.

5.1 Halo shape

To characterize the shape of DM haloes, we study the following quantities derived from the three eigenvalues ($a \geq b \geq c$) of the inertia tensor, as calculated by the AMIGA *halo finder*:

(i) sphericity: c/a
(ii) elongation: b/a
(iii) triaxiality: $(a^2 - b^2)/(a^2 - c^2)$.

In Fig. 7 , we plot the sphericity measured from the sample set of relaxed haloes. We observe no significant deviation from CDM for WDM, γCDM or νCDM. The same is true for the elongation and triaxiality, and for different redshifts and interaction cross-sections. Thus, we cannot distinguish these models by the shape of their DM haloes.
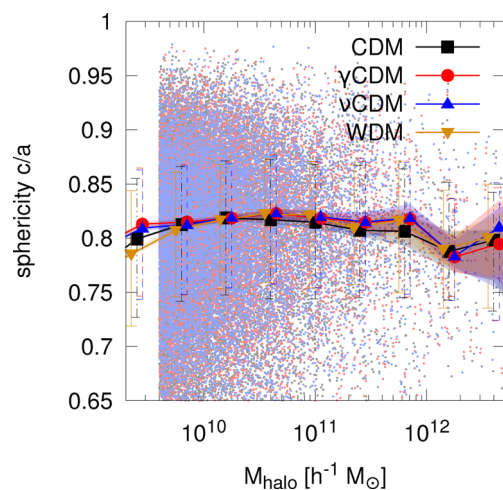
Figure 7. Sphericity of relaxed DM haloes for CDM, γCDM, νCDM and WDM at redshift $z = 0$. The symbols show the sphericity in mass bins ranging from 4×10^9 to $10^{11} \, h^{-1} \, \mathrm{M_\odot}$ for the different models as labelled. The shaded areas indicate the 95 per cent CL on the median, given the underlying scatter in the halo sample set (small dots), while the error bars mark the 20–80 per cent interval for this distribution. The sphericity of DM haloes measured in WDM, γCDM and νCDM shows no significant deviation from CDM.

5.2 Density profile and concentration

To analyse the density profiles of DM haloes, we first average the density in shells around the centre of mass for all haloes in a given mass bin. A comparison of the results with a fitted NFW profile (Navarro, Frenk & White 1997) reveals a sufficiently good agreement to justify parameterizing the halo profiles in this way.[8] The NFW profile is completely characterized by the concentration parameter, c_{NFW}, which is determined by the halo finder using the approximation presented in Prada et al. (2012).

In Fig. 8, we plot the concentration versus mass, cross-section and redshift relations. We observe a significantly lower median value of c_{NFW} in the mass bins below the half-mode mass for γCDM and νCDM compared to CDM. This reduction in concentration with increasing interaction cross-section is similar to the effect seen in WDM simulations with reducing particle mass, which has been explained as being due to the delayed formation time of low-mass haloes (Lovell et al. 2012). At these late times, the interacting DM models become (effectively) non-collisional for the cross-sections studied here, in the same way that free-streaming in WDM models becomes negligible at low redshifts. Therefore, it is valid to assume that this lower concentration also originates from the later collapse of the DM haloes in these models.

As we increase the interaction cross-section, the deviation from CDM becomes larger due to an increase in the mass scale of the suppression. Since we have fixed the mass interval, the median concentration decreases as a larger number of high-mass haloes become affected.

---

[7] We omit the substructure mass fraction criterion as this is strongly correlated with the centre-of-mass displacement criterion listed (Neto et al. 2007).

[8] The fit starts at a minimum radius from the halo centre as defined by Power et al. (2003) to ensure convergence of the density profile.
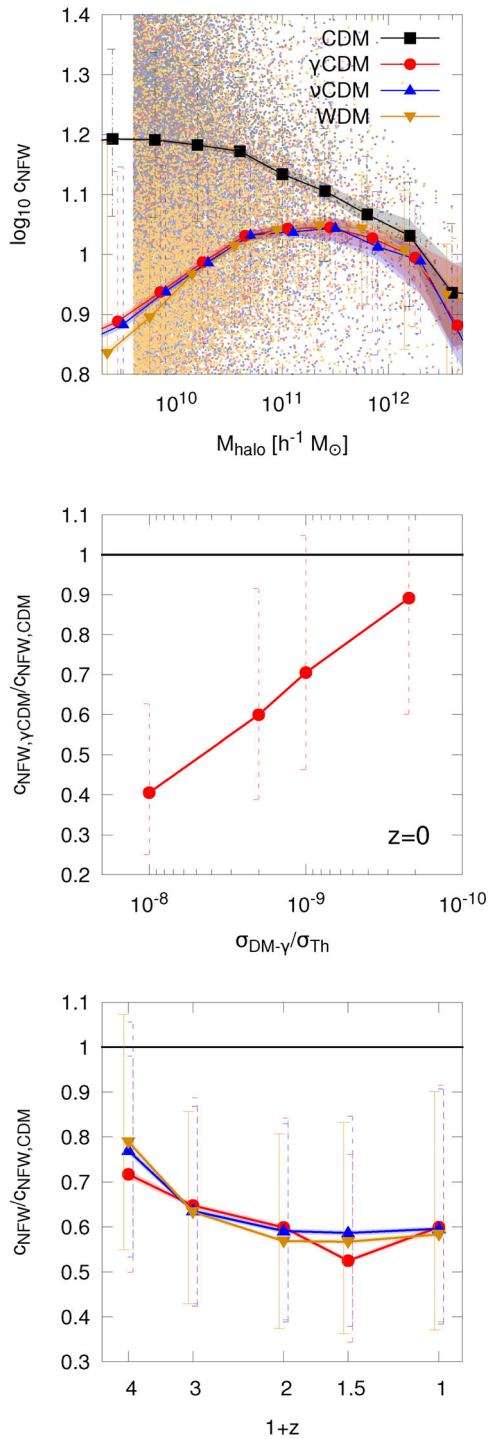
Figure 8. The concentration–mass relation (top) shows a strong mass-dependence for γCDM, νCDM and WDM, which develops at scales below $\sim 10^{11}\,h^{-1}\,\mathrm{M}_\odot$. These models are indistinguishable from CDM for more massive haloes. This deviation in the concentration depends strongly on the interaction cross-section (middle) and becomes slightly smaller at higher redshifts (bottom). The data points are the median values for the mass bins ranging from 4×10^9 to $10^{11}\,h^{-1}\,\mathrm{M}_\odot$, while the shaded regions mark the 95 per cent CL on the median, given the underlying scatter in the halo sample set (small dots in the top plot). The error bars mark the 20–80 per cent interval for this distribution.

5.3 Halo spin

We quantify the spin of DM haloes using the 'classical' definition of Peebles (1969),

$$\lambda = \frac{J|E|^{1/2}}{GM_{\mathrm{vir}}^{5/2}}, \tag{17}$$

where J and E are, respectively, the total angular momentum and binding energy of the material within the virial mass, M_{vir}, of a halo.

In the linear and quasi-linear regime, halo spin is described reasonably well using *tidal torque theory* (hereafter TTT; White 1984) and originates from tidal interactions between collapsing haloes. In this framework, the angular momentum of a (proto)galaxy depends on the mass, but also weakly on the formation time. However, it should be noted that comparisons with numerical simulations have revealed that TTT becomes less applicable as haloes approach turn-around and virialization (Porciani, Dekel & Hoffman 2002). It is still an open question whether haloes acquire significant angular momentum due to mergers with other haloes, as well as from tidal torques (Maller, Dekel & Somerville 2002; D'Onghia & Navarro 2007).

In Fig. 9, we plot the median halo spin against virial mass for the different models. We find a similar reduction and evolution of halo spin for γCDM, νCDM and WDM, compared to CDM.
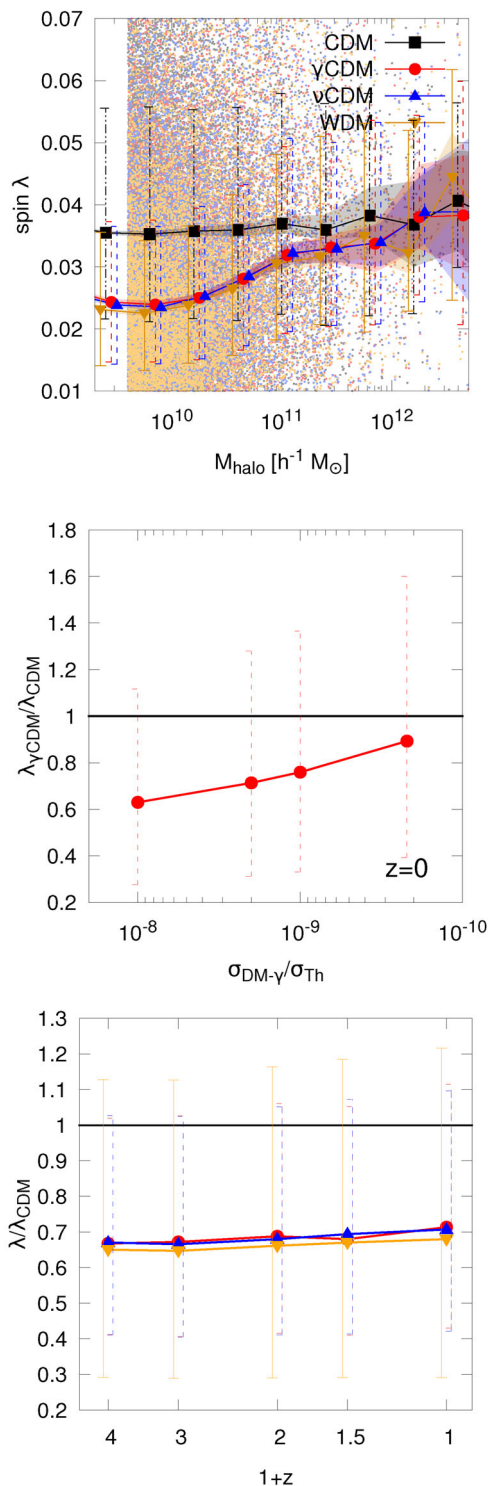
There are various explanations for the difference in halo spin with respect to CDM. As this effect is seen for haloes consisting of more than a few thousand particles, we can rule out a numerical convergence problem. If it originates solely from tidal torques, then the weak dependence of angular momentum on formation time would yield a smaller spin for the earlier formation time found. If mergers are responsible for spinning up haloes, then the lack of smaller progenitors of low-mass haloes and consequently, smoother accretion on to these haloes in γCDM, νCDM and WDM, would also result in a lower net spin. The fact that the difference remains constant over time while the absolute value grows, seems to support the idea that not only the initial tidal torque on the collapsing structure, but also the environment at late times, influences the spin.

6 CONCLUSION

We have shown that even relatively weak DM–radiation interactions can alter SF on small cosmic scales. In Boehm et al. (2014), we showed that the number of Milky Way satellites is reduced when DM has primordial interactions with photons (γCDM) or neutrinos (νCDM) and that the resulting number of satellites can be used to place constraints on the interaction cross-section. In this paper, we have extended our previous analysis to study the abundance of DM haloes and their internal properties, namely their shape, density profile and spin. We have also compared different models (γCDM, νCDM and WDM) in which the power spectrum of density fluctuations is suppressed on small scales.

The HMFs measured in our simulations show that the γCDM and νCDM models contain more haloes than WDM around a mass of $10^9\,h^{-1}\,\mathrm{M}_\odot$ for the parameters considered here. This behaviour is not reproduced by various semi-analytical descriptions of the HMF. We note that these mass scales are an order of magnitude larger than the scale on which spurious haloes are expected to make a significant contribution (Wang & White 2007). The source of this overabundance of haloes with respect to WDM needs to be addressed but could be due to the choice of models for the initial conditions in WDM.

Both the NFW concentration parameter in the density profile and the spin show departures from CDM for low-mass haloes. The halo shape, on the other hand, is independent of the DM model. The lower halo concentration and angular momentum may be due to the delayed formation time of low-mass haloes in γCDM and νCDM and are similar to the trends seen in WDM. However, it should be noted that these halo properties do not provide a means to distinguish between γCDM, νCDM and WDM.

Ideally, the next step in this study would be to include baryonic physics in our simulations, which may have an impact on some of the results reported in our DM-only simulations. Bryan et al. (2013) have shown that efficient gas cooling results in an increased halo spin, while AGN feedback counters this trend. The mass–concentration relation of the haloes is very similar when baryons are included (Schaller et al. 2014) and the baryons only affect the radial density profile of the inner core within 5 per cent of the virial radius, producing a contraction. Recent studies also include a possible coupling of DM with dark radiation (Buckley et al. 2014), which leads to a similar suppression of initial fluctuations as seen in our models and, depending on the cross-section, should give rise to similar results as those discussed in this paper.

REFERENCES

Agarwal S., Corasaniti P. S., Das S., Rasera Y., 2014, preprint (arXiv:1412.1103)
Angulo R., Baugh C., Lacey C., 2008, MNRAS, 387, 921
Benson A. J. et al., 2013, MNRAS, 428, 1774
Bertoni B., Ipek S., McKeen D., Nelson A. E., 2014, preprint (arXiv:1412.3113)
Bode P., Ostriker J. P., Turok N., 2001, ApJ, 556, 93
Boehm C., Schaeffer R., 2005, A&A, 438, 419
Boehm C., Fayet P., Schaeffer R., 2001, Phys. Lett. B, 518, 8
Boehm C., Riazuelo A., Hansen S. H., Schaeffer R., 2002, Phys. Rev. D, 66, 083505
Boehm C., Schewtschenko J., Wilkinson R., Baugh C., Pascoli S., 2014, MNRAS, 445, L31
Boyanovsky D., Wu J., 2011, Phys. Rev. D, 83, 043524
Boylan-Kolchin M., Bullock J. S., Kaplinghat M., 2011, MNRAS, 415, L40
Bryan S. E., Kay S. T., Duffy A. R., Schaye J., Dalla Vecchia C., Booth C. M., 2013, MNRAS, 429, 3316
Buckley M. R., Zavala J., Cyr-Racine F.-Y., Sigurdson K., Vogelsberger M., 2014, Phys. Rev. D, 90, 043524
Chu X., Dasgupta B., 2014, Phys. Rev. Lett., 113, 161301

Figure 9. The spin–mass relation (top) shows a mass-dependence for γCDM, νCDM and WDM, which develops at scales below $\sim 10^{11}\,h^{-1}\,\mathrm{M_\odot}$. These models are indistinguishable from CDM for more massive haloes. This spin reduction on small scales depends on the interaction cross-section (middle) while the relative deviation from collisionless CDM remains constant over time (bottom). The data points are the median values for the mass bins ranging from 4×10^9 to $10^{11}\,h^{-1}\,\mathrm{M_\odot}$, while the shaded regions mark the 95 per cent CL on the median, given the underlying scatter in the halo sample set (small dots in the top plot). The error bars mark the 20–80 per cent interval for this distribution.

Crocce M., Pueblas S., Scoccimarro R., 2012, available at: http://cosmo.nyu.edu/roman/2LPT/

Cyr-Racine F.-Y., Sigurdson K., 2013, Phys. Rev. D, 87, 103515

D'Onghia E., Navarro J. F., 2007, MNRAS, 380, 58

Davis M., Efstathiou G., Frenk C. S., White S. D., 1985, ApJ, 292, 371

Dolgov A., Dubovsky S., Rubtsov G., Tkachev I., 2013, Phys. Rev. D, 88, 117701

Jenkins A., Frenk C. S., White S. D. M., Colberg J. M., Cole S., Evrard A. E., Couchman H. M. P., Yoshida N., 2001, MNRAS, 321, 372

Klypin A. A., Kravtsov A. V., Valenzuela O., Prada F., 1999, ApJ, 522, 82

Knollmann S. R., Knebe A., 2009, ApJS, 182, 608

Lacey C. G., Cole S., 1993, MNRAS, 262, 627

Lesgourgues J., 2011, preprint (arXiv:1104.2932)

Lovell M. R. et al., 2012, MNRAS, 420, 2318

Lovell M. R., Frenk C. S., Eke V. R., Jenkins A., Gao L., Theuns T., 2014, MNRAS, 439, 300

Maccio' A. V., Dutton A. A., van den Bosch F. C., Moore B., Potter D., Stadel J., 2007, MNRAS, 378, 55

Maller A. H., Dekel A., Somerville R. S., 2002, MNRAS, 329, 423

Mangano G., Melchiorri A., Serra P., Cooray A., Kamionkowski M., 2006, Phys. Rev. D, 74, 043517

Moore B., Ghigna S., Governato F., Lake G., Quinn T. R., Stadel J., Tozzi P., 1999, ApJ, 524, L19

Navarro J. F., Frenk C. S., White S. D., 1997, ApJ, 490, 493

Neto A. F. et al., 2007, MNRAS, 381, 1450

Peebles P., 1969, ApJ, 155, 393

Planck Collaboration XVI , 2014, A&A, 571, A16

Porciani C., Dekel A., Hoffman Y., 2002, MNRAS, 332, 339

Power C., Navarro J. F., Jenkins A., Frenk C. S., White S. D. M., Springel V., Stadel J., Quinn T., 2003, MNRAS, 338, 14

Prada F., Klypin A. A., Cuesta A. J., Betancort-Rijo J. E., Primack J., 2012, MNRAS, 428, 3018

Press W. H., Schechter P., 1974, ApJ, 187, 425

Rocha M., Peter A. H., Bullock J. S., Kaplinghat M., Garrison-Kimmel S., Oñorbe J., Moustakas L. A., 2013, MNRAS, 430, 81

Schaeffer R., Silk J., 1988, ApJ, 332, 1

Schaller M., Frenk C. S., Bower R. G., Theuns T., Jenkins A. et al., 2014, preprint (arXiv:1409.8617)

Schneider A., 2014, preprint (arXiv:1412.2133)

Schneider A., Smith R. E., Macciò A. V., Moore B., 2012, MNRAS, 424, 684

Schneider A., Smith R. E., Reed D., 2013, MNRAS, 433, 1573

Serra P., Zalamea F., Cooray A., Mangano G., Melchiorri A., 2010, Phys. Rev. D, 81, 043507

Sheth R. K., Mo H., Tormen G., 2001, MNRAS, 323, 1

Sigurdson K., Doran M., Kurylov A., Caldwell R. R., Kamionkowski M., 2004, Phys. Rev. D, 70, 083501

Springel V., 2005, MNRAS, 364, 1105

Viel M., Lesgourgues J., Haehnelt M. G., Matarrese S., Riotto A., 2005, Phys. Rev. D, 71, 063534

Vogelsberger M., Zavala J., Simpson C., Jenkins A., 2014, MNRAS, 444, 3684

Wang J., White S. D., 2007, MNRAS, 380, 93

Wang M.-Y., Peter A. H. G., Strigari L. E., Zentner A. R., Arant B., Garrison-Kimmel S., Rocha M., 2014, MNRAS, 445, 614

White S., 1984, ApJ, 286, 38

Wilkinson R. J., Boehm C., Lesgourgues J., 2014a, J. Cosmol. Astropart. Phys., 1404, 026

Wilkinson R. J., Boehm C., Lesgourgues J., 2014b, J. Cosmol. Astropart. Phys., 1405, 011

This paper has been typeset from a TeX/LaTeX file prepared by the author.